HI^2: Sparse-View 3D Object Reconstruction with a Hybrid Implicit Initialization

Pragati Jaiswal[1,2] and Didier Stricker[1,2]
[1]*RPTU - Technische Universität Kaiserslautern*
[2]*DFKI – German Research Center for Artificial Intelligence*
pragati.jaiswal@dfki.de, didier.stricker@dfki.de

Keywords: Object Reconstruction, 3D Reconstruction, Hybrid Implicit Initialization

Abstract: Accurate 3D object reconstruction is essential for various applications, including mixed reality and medicine. Recent advancements in deep learning-based methods and implicit 3D modelling have significantly enhanced the accuracy of 3D object reconstruction. Traditional methods enable reconstruction from a limited number of images, while implicit 3D modelling is proficient at capturing fine details and complex topologies. In this paper, we present a novel pipeline for 3D object reconstruction that combines the strengths of both approaches. Firstly, we use a 3D occupancy grid to generate a coarse 3D object from a few images. Secondly, we implement a novel and effective sampling strategy to transform the coarse reconstruction into an implicit representation, which is optimized to reduce computation power and training time. This sampling strategy also allows it to be true to scale given actual camera intrinsic and extrinsic parameters. Finally, we refine the implicit representation and extract the 3D object mesh under a differentiable rendering scheme. Experiments on several datasets demonstrate that our proposed approach can reconstruct accurate 3D objects and outperforms state-of-the-art methods in terms of the Chamfer distance and Peak Signal-to-Noise Ratio metrics.

1 INTRODUCTION

The topic of 3D object reconstruction has received increased attention due to the recent emergence of many neural implicit representations. The ability to easily reconstruct even photorealistic 3D objects is of significant interest for a wide field of applications. This is especially the case in the field of virtual and augmented reality. However, not all of these methods produce an output that is compatible with standard rendering engines. Some representations like neural radiance fields (Mildenhall et al., 2021) and voxel grids (Fridovich-Keil et al., 2022) require a volume rendering approach that can be very costly. In those cases, it might not be possible to achieve real-time rendering unless a mesh is extracted in a separate step. Converting these representations in a separate step is, however, computationally expensive and can reduce the quality of the original reconstruction. Methods that directly output a mesh are, therefore, preferable as they do not require additional computations and retain their level of quality. In this work, we aim to reconstruct high-fidelity 3D models of objects using only a sparse set of images. The implicit modelling is suitable for capturing high-frequency details. Meanwhile, a coarse mesh makes the reconstruction from a few images possible. Motivated by this, we propose a novel 3D object reconstruction pipeline HI^2, combining the strengths of implicit modelling and explicit coarse mesh reconstruction. For this, we use a novel approach to create a coarse reconstruction of the ob-

Figure 1: We propose HI^2, a novel Hybrid Implicit Initialization. Given sparse views, we aim to reconstruct a highly accurate mesh of the object. In this figure, we show input images and our 3D object reconstruction. It is clearly noticeable that our reconstruction pipeline can maintain high-frequency details.

ject from as few as five images.

We then optimize this initial mesh using implicit modelling via a neural rendering-based optimization process. We propose a novel shell-constrained sampling strategy to transfer the coarse reconstruction into an implicit representation. Thanks to this shell, we are able to sample only from the area close to the object's surface instead of sampling from all points in the unit cube, as most approaches do (Park et al., 2019; Tretschk et al., 2020). Using the sampled Signed Distance Function (SDF) values, we initialize a differentiable tetrahedral grid (Shen et al., 2021). By combining the differentiable implicit representation with texture and lightning modelling (Munkberg et al., 2022), we optimize the tetrahedral grid w.r.t. the photometric reprojection error. Finally, we directly extract the object surface from the tetrahedral grid without the expensive computational overhead. We successfully lifted the implicit modelling to a 3D reconstruction from sparse views using our pipeline.

We can summarize our main contributions as follows:

- We introduce an approach that combines classic 3D occupancy mapping and implicit 3D modelling for 3D object reconstruction.
- We propose a novel shell-constrained sampling strategy which helps in reducing the required computational power and training time. In addition, it helps in generating a high-quality mesh even with a limited number of images.

Extensive experiments demonstrate that our pipeline can reconstruct a full 3D object with rich details using only a few images. We also show that we outperform State-Of-The-Art (SOTA) implicit 3D modelling approaches w.r.t. the Chamfer distance metric and Peak Signal-to-Noise Ratio (PSNR) under different numbers of views.

2 RELATED WORK

2.1 Classical Methods

Multi-View Stereo (MVS) is a fundamental problem in 3D computer vision and has been extensively researched. The classic approaches usually estimate the depth map through matching correspondences across images (Pons et al., 2005; Kolmogorov and Zabih, 2002; Goesele et al., 2006). However, the matching quality heavily depends on the degree of overlap in the neighbourhood images, which requires a large number of views. Although such approaches have achieved a promising reconstruction quality (Furukawa and Ponce, 2009; Galliani et al., 2016; Schönberger et al., 2016), the dense matching and the post-processing step for mesh generation (Kazhdan et al., 2006) are computationally expensive.

2.2 Explicit Representations

With the development of deep learning, MVS can easily become more feasible by implementing learning-based components for the subtasks, such as feature matching (Hartmann et al., 2017; Luo et al., 2019) and depth fusion (Donne and Geiger, 2019; Riegler et al., 2017). Furthermore, end-to-end deep learning approaches are also proposed to directly reconstruct objects from input images. A research branch reconstructs the object in voxel-grids (Choy et al., 2016; Kar et al., 2017; Yan et al., 2016). However, the voxel-grid size grows cubically to maintain fine details in the reconstruction. Moreover, the voxel representation is incompatible with the standard rendering pipeline, limiting their applications in graphics. Presenting object shapes as a mesh in the reconstruction is more memory efficient. Nevertheless, most approaches assume a fixed mesh topology (Wang et al., 2018; Liu et al., 2019a; Kanazawa et al., 2018), which makes those approaches only suitable for reconstructing objects with similar geometries.

2.3 Implicit Representations

A more memory-efficient way is to represent the object surface as neural implicit representations, which can theoretically express the object surface in an infinite resolution with a fixed memory demand. SDF (Park et al., 2019) and occupancy functions (Mescheder et al., 2019) are commonly used as neural implicit representations. In multi-view 3D reconstruction, neural implicit representations are mostly used jointly with differentiable rendering (Jiang et al., 2020; Liu et al., 2020; Liu et al., 2019b) to extract the surface point of each view. Implicit Differentiable Renderer (IDR) (Yariv et al., 2020) further combines the implicit representation with the apprentice model that can differentiably render object views accounting for light effects. Thanks to the differentiable modelling of object geometry and appearance, IDR is able to reconstruct high-quality object surfaces under 2D supervision only. However, IDR still relies on the computationally expensive Marching Cubes algorithm (Lorensen and Cline, 1987) to extract the reconstructed object surface. Instead, Deep Marching Tetrahedra (DMTet) (Shen et al., 2021) proposes a novel 3D representation to re-

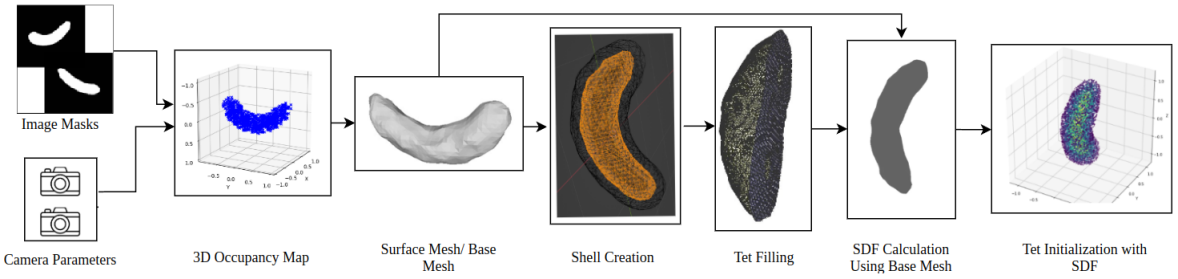

Figure 2: **Hybrid Implicit Initialization (HI^2)**. Our initialization approach starts from a sparse set of images to reconstruct a coarse mesh using a 3D occupancy map. A shell is then constructed around the coarse mesh, which is filled with a tetrahedral grid. Additionally, a Signed Distance Function (SDF) is created using the tetrahedral grid and coarse mesh.

construct the shape by a differentiable marching tetrahedra layer while keeping a fast inference rate. Nvdiffrec (Munkberg et al., 2022) implements a reconstruction pipeline upon DMTet with additional materials and lighting modelling, which takes a step further towards high-fidelity 3D reconstruction from images. Neural volumes can also be seen as a 3D object representation. With volumetric rendering, Neural Radiance Fields (NeRF) (Mildenhall et al., 2021) and its follow-up work (Garbin et al., 2021; Martin-Brualla et al., 2021; Pumarola et al., 2021; Reiser et al., 2021; Wang et al., 2021; Wizadwongsa et al., 2021; Yu et al., 2021; Zhang et al., 2020; Kellnhofer et al., 2021) have shown great success in the area of novel view synthesis. However, they are mainly focused on the optimization of object appearance. The ambiguity in the volumetric rendering limits the supervision of the object geometry (Zhang et al., 2020). Although one can also extract object surfaces from such methods, the reconstructed geometry is usually not satisfiable.

Our approach builds on the advances of DMTet and Nvdiffrec through a clever hybrid initialization that takes advantage of explicit and implicit representations.

3 METHOD

We present a method for 3D object reconstruction that utilizes a sparse set of images of an arbitrary object. Starting with a minimum of five input images, accompanied by masks and camera parameters, we generate a 3D occupancy map of the object. This occupancy map serves as the foundation for reconstructing a coarse mesh, which forms the initial structure of our method.

Next, we refine the reconstruction by creating a shell around the coarse mesh and filling it with a tetrahedral grid. Unlike arbitrary shapes, the shell-constrained tetrahedral grid closely approximates the object's structure, providing a more accurate starting point for further optimization.

The tetrahedral mesh is initialized with SDF values derived from the coarse mesh. Using this initialized mesh, we employ the Nvdiffrec's DMTet pipeline to optimize the reconstruction. During each optimization iteration, the tetrahedral mesh is differentiably rendered, allowing us to compute the loss between the rendered image and the ground truth inputs.

3.1 Initialization Approach

In the following, we detail the steps of our initialization approach, summarized in Figure 2.

3.1.1 Coarse Mesh

Given a set of posed colour images $I = \{I_1, I_2, \ldots, I_N\}$ with corresponding binary object masks $\mathcal{M} = \{M_1, M_2, \ldots, M_N\}$ and known camera parameters $\mathcal{C} = \{C_1, C_2, \ldots, C_N\}$, we estimate a coarse occupancy map of the object using a space carving algorithm (Kutulakos and Seitz, 2000).

A set of random 3D points $\mathcal{P} = \{\mathbf{p}_1, \mathbf{p}_2, \ldots, \mathbf{p}_K\}$, where $\mathbf{p}_i = (x_i, y_i, z_i)$, is generated within the 3D space enclosing the object. Each point is projected onto the 2D image plane of every view $n \in [1, N]$ using the camera projection function P_n, defined as:

$$u, v = P_n(\mathbf{p}_i, C_n) = \left(\frac{f_x x_i}{z_i} + c_x, \frac{f_y y_i}{z_i} + c_y \right), \quad (1)$$

where f_x, f_y are the focal lengths, and c_x, c_y are the principal points.

For each projected point, we check if its projection (u, v) lies within the object mask $M_n(u, v)$:

$$o_n(\mathbf{p}_i) = \begin{cases} 1 & \text{if } M_n(u, v) = 1, \\ 0 & \text{otherwise.} \end{cases} \quad (2)$$

The object's final occupancy score is determined by aggregating $o_n(\mathbf{p}_i)$ across all views:

$$O(\mathbf{p}_i) = \frac{1}{N} \sum_{n=1}^{N} o_n(\mathbf{p}_i) \quad (3)$$

Points with $O(\mathbf{p}_i) \geq \tau$, where τ is a threshold (e.g., $\tau = 0.5$), are retained as part of the object's visual hull.

An alpha shape $\mathcal{A}_\alpha$ is computed from the retained points, representing the coarse mesh. The alpha shape is defined as the smallest triangulation enclosing the points such that all edges have a length $\leq \alpha$. The choice of α is influenced by the approximate spacing between the points d_{mean}, which depends on the density of the initialized point cloud.

$$\alpha \approx c \cdot d_{mean} \tag{4}$$

where c is a scaling factor typically in range $1.5 \leq c \leq 3$, depending on desired granularity. This shape approximates the object's geometry and provides a coarse mesh for subsequent steps.

3.1.2 Tetrahedral Mesh

Using the coarse mesh $\mathcal{A}_\alpha$, we generate a tetrahedral mesh $\mathcal{T}$ using the Quartet framework (Bridson and Doran, 2014). Quartet employs an isosurface stuffing algorithm (Shewchuk, 1998), which generates a tetrahedral grid from a defined boundary.

Instead of generating a tetrahedral grid within a unit cube, we focus mesh generation on the near-surface regions of the coarse mesh.

A conforming shell $\mathcal{S}_\delta$ with thickness δ is constructed around $\mathcal{A}_\alpha$:

$$\mathcal{S}_\delta = \{\mathbf{q} \mid \mathbf{q} \in \mathbb{R}^3,\, d(\mathbf{q}, \mathcal{A}_\alpha) \leq \frac{\delta}{2}\}, \tag{5}$$

where $d(\mathbf{q}, \mathcal{A}_\alpha)$ is the Euclidean distance from $\mathbf{q}$ to the nearest point on $\mathcal{A}_\alpha$.

The shell $\mathcal{S}_\delta$ serves as the input boundary for the Quartet framework, ensuring that the tetrahedral mesh $\mathcal{T}$ aligns closely with the object's surface geometry.

3.1.3 Signed Distance Function (SDF)

To improve convergence and guide optimization, we initialize the tetrahedral mesh with SDF values derived from the coarse mesh.

For each vertex $\mathbf{v}_i \in \mathcal{T}$, the SDF value is computed as:

$$\text{SDF}(\mathbf{v}_i) = \text{sgn}(\mathbf{v}_i) \cdot \min_{\mathbf{p} \in \mathcal{A}_\alpha} \|\mathbf{v}_i - \mathbf{p}\|_2, \tag{6}$$

where $\text{sgn}(\mathbf{v}_i) = -1$ if $\mathbf{v}_i$ is inside the coarse mesh and $+1$ otherwise.

The computed SDF values initialize the tetrahedral grid, encoding proximity to the object's surface. This initialization provides:

- **Improved Geometry Awareness:** The optimization starts with a spatially informed structure.
- **Faster Convergence:** A better initial configuration reduces the number of iterations required for optimization.

By combining these mathematically grounded steps, our initialization approach achieves robust and efficient 3D object reconstruction, even with sparse input data. The method ensures high fidelity while maintaining computational efficiency.

3.2 3D Reconstruction

The next stage focuses on refining and optimizing the mesh geometry to align with the input images, thereby improving the overall representation of the reconstructed object. A visualization of this reconstruction pipeline is provided in Figure. 3.

To achieve this, we utilize the DMTet framework, integrated with 2D supervision from Nvdiffrec. This integration enables efficient optimization of the mesh geometry. Unlike other approaches such as IDR, which treat geometry and material properties as separate components, Nvdiffrec jointly optimizes geometry, materials, and lighting. This simultaneous optimization enhances the alignment between the reconstructed shape and the image data, leading to a more robust reconstruction process.

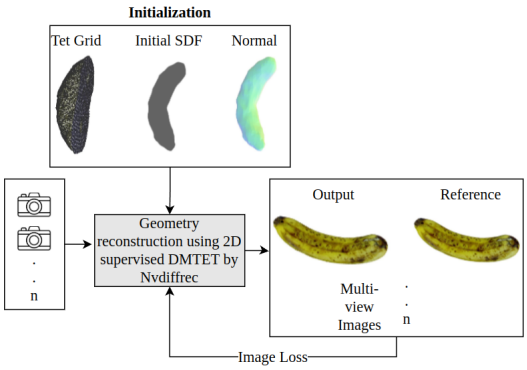

Figure 3: Reconstruction pipeline with HI^2: Multiview images and their corresponding camera parameters serve as input. Our initialization approach is used to enhance the DMTet framework, supervised by Nvdiffrec, for improved 3D object reconstruction.

3.2.1 Optimization Process

During each iteration of the optimization, the marching tetrahedral layer is converted into a surface mesh representation. This surface mesh is rendered using a differentiable rasterizer, utilizing the provided camera parameters and viewpoints. The rendered output is compared against the ground truth image data to compute a loss function in the image space. This loss is backpropagated through the optimization pipeline, enabling updates to the surface mesh embedded in the implicit field.

The iterative refinement involves two key components:

- **Vertex Adjustments:** The positions of vertices within the tetrahedral grid are updated to improve the alignment of the mesh with the object's true geometry.
- **SDF Updates:** The SDF values associated with the tetrahedral mesh are also refined, ensuring the implicit representation more accurately encodes the object's shape.

By integrating our SDF-derived initialization, the DMTet framework begins optimization from a well-informed starting point. This initialization incorporates spatial information about the object's geometry, leading to faster convergence and improved accuracy. The SDF initialization reduces the dependency on extensive input data, allowing our method to produce high-quality 3D reconstructions with a sparse set of input images.

This combination of SDF-based initialization and joint optimization of geometry, materials, and lighting ensures the reconstructed 3D mesh achieves a high level of fidelity, even in scenarios with limited input.

4 EXPERIMENTS

4.1 Dataset

To evaluate the performance and versatility of our proposed method, we utilized the OmniObject3D (Wu et al., 2023) dataset and a synthetic face dataset created specifically for this study. These datasets were chosen to ensure a robust assessment across a diverse range of object types, including both general and highly specialized geometries.

4.1.1 OmniObject3D

The OmniObject3D dataset provides an extensive collection of object categories with varying shapes and complexities. It serves as a benchmark for testing our method's capability to reconstruct a wide variety of objects, from simple to highly intricate geometries. By leveraging this dataset, we validate the robustness and generalizability of our approach across general object types.

4.1.2 Synthetic Face Dataset

To further demonstrate the flexibility of our method, particularly for objects with intricate geometry, we developed a synthetic face dataset. This dataset was created by rendering 3D models using CharacterCreator4 (Inc., 2022) in Blender (Community, 2018). The dataset includes three distinct 3D models:

- One female model.
- Two male models, one with hair and the other bald, to evaluate the reconstruction performance across different head geometries, including variations with long, short, or no hair.

To increase the difficulty and simulate diverse viewing conditions, we rendered images along a camera arc spanning -90° to $+90^\circ$. Figure 4 shows the starting and ending position of the camera's arc. All images were generated under consistent lighting and rendering settings to maintain controlled experimental conditions.

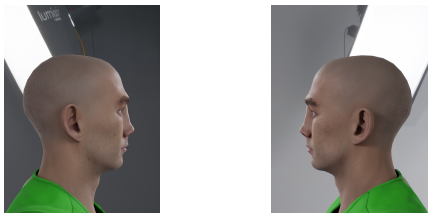

(a) Starting Position (b) Ending Position

Figure 4: Visualization of the camera arc: (a) Starting position of the camera; (b) Ending position of the camera, demonstrating the range used in the experiments.

4.2 Evaluation Setup

By combining the OmniObject3D dataset with the synthetic face dataset, we comprehensively evaluate our method's ability to handle diverse object categories and geometries. OmniObject3D ensures the general applicability of the method, while the synthetic face dataset tests its robustness on highly detailed and geometrically complex objects such as human faces.

We maintained consistent evaluation parameters for all methods we tested. The resultant 3D mesh is aligned with the ground truth mesh using landmarks and then fine-tuned using Trimesh (Dawson-Haggerty et al.,) implementation of the Iterative Closest Point (ICP) (Besl and McKay, 1992). Our comparison of results against other methods was done by using unidirectional Chamfer distance.

Our evaluation involved comparing the 3D mesh predictions from Nvdiffrec and IDR trained on the same dataset across different views. For the OmniObject3D dataset, we had a full dataset (100 images) as well as randomly chosen subsets containing 20, 10, and 5 images. To ensure a fair comparison, the same subsets were used for evaluating each method. We used 19, 13, 9, and 5 images for the

face dataset. This comprehensive comparison allowed us to understand how the performance of Nvdiffrec, IDR and our method trained on identical datasets, varied under different training datasets and number of views. Additionally, we conducted a comparative analysis between the outcomes produced by Nvdiffrec and our initialization strategy. This comparison aimed to assess the convergence of the two methods. We achieved this by contrasting the Peak Signal-to-Noise Ratio (PSNR) and the Mean Squared Loss (MSE) calculated between the input image and the rendered image at different numbers of training epochs. This evaluation allowed us to gauge the effectiveness of our initialization approach in relation to Nvdiffrec's performance.

4.3 Ablation Study

We perform an ablation study on the size of tets used for filling the shell created. We start by filling the shell with a tet size of 0.007, 0.005, and 0.003 respectively. We observe that the smaller the size of the tet grid used for the generation, the higher the high-frequency detail which can be observed in Figure 5, especially if we look closer at the eye region and hair. However,

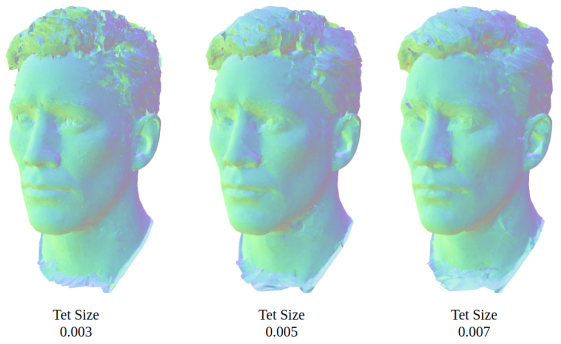

Figure 5: Visual comparison of 3D reconstructions with different tet sizes. As the tet size increases, the level of detail in the reconstructed surface changes, with a finer tet size (0.003) capturing sharper geometric details, while a larger tet size (0.007) results in smoother reconstructions.

we also note that smaller tet sizes result in noisier and less smooth surfaces in the 3D model, potentially detracting from the overall realism. Conversely, while larger tet sizes, such as 0.007, produce smoother surfaces, they lack the finer detail captured by smaller tet sizes.

The results as visualized in Figure 6, further support this observation. At a tet size of 0.005, we observe an optimal balance between PSNR and MSE, indicating that it achieves a good trade-off between capturing sufficient detail and maintaining surface smoothness. This balance makes 0.005 an ideal

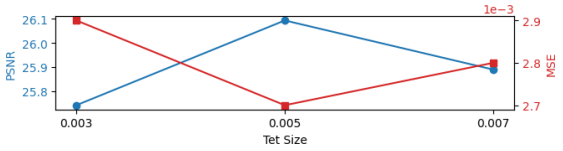

Figure 6: Effect of tet size on PSNR and MSE. The blue curve represents PSNR values (left axis), and the red curve represents MSE values (right axis).

choice for maintaining both visual quality and realism in the reconstructed model.

4.4 Quantitative Results

4.4.1 HI^2 vs Nvdiffrec

In Figure 7, it is evident that HI^2 achieves convergence with only a few training iterations. This is indicated not only by the better PSNR and MSE values but also by the clear convergence in the graph. The number of training iterations required is directly related to the training time, and the proposed reconstruction pipeline requires less training time than Nvdiffrec with the standard random tet grid initialization for 3D object reconstruction.

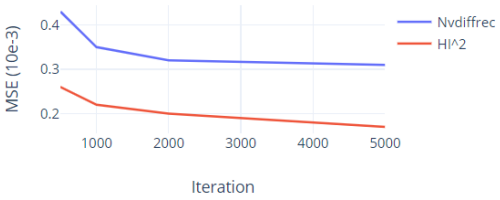

(a) MSE ↓ vs No. of iterations

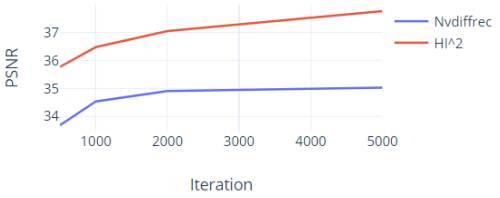

(b) PSNR ↑ vs No. of iterations

Figure 7: Comparison between Nvdiffrec with standard random tet grid initialization and HI^2. HI^2 converges better than Nvdiffrec with standard random tet grid initialization.

4.4.2 HI^2 vs All

We compare HI^2 against Nvdiffrec and IDR across diverse 3D object reconstruction tasks. Table 1 shows that HI^2 consistently outperforms all methods in terms of Chamfer distance across different datasets

	Anise				Banana				Face-1				Face-2				Face-3			
Views	5	10	20	100	5	10	20	100	5	9	13	19	5	9	13	19	5	9	13	19
Nvdiffrec	0.019	0.016	0.015	0.014	0.018	0.014	0.014	0.014	0.011	0.009	0.009	0.009	0.012	0.011	0.012	0.011	0.012	0.011	0.011	0.011
IDR	0.022	0.013	0.009	0.005	0.006	0.005	0.006	0.004	0.025	0.025	0.024	0.024	0.042	0.029	0.026	0.030	0.029	0.029	0.029	0.029
HI^2	**0.008**	**0.006**	**0.005**	**0.004**	**0.005**	**0.004**	**0.004**	**0.001**	**0.008**	**0.008**	**0.008**	**0.008**	**0.010**	**0.010**	**0.010**	**0.010**	**0.010**	**0.010**	**0.010**	**0.010**

Table 1: Chamfer distance ↓ comparison for OmniObject3D and face datasets across various number of views. The bolded values indicate the best performance for each dataset and view count combination.

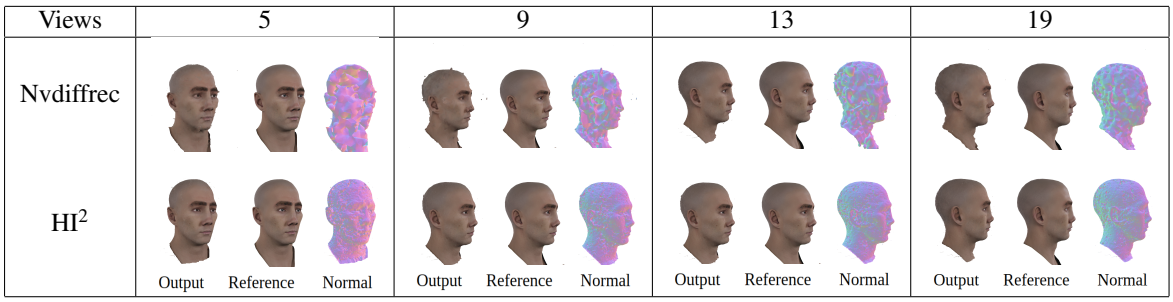

Figure 8: Convergence of 3D reconstruction in 100 iterations with different numbers of views, using Nvdiffrec vs. HI^2.

and numbers of input views.

HI^2 achieves the lowest Chamfer distance across all object categories, with smaller values indicating better performance. Notably, it excels with sparse input (e.g., 5 views), delivering significantly lower Chamfer distances than IDR and Nvdiffrec, demonstrating its efficiency when there is limited data available.

4.5 Qualitative Results

4.5.1 HI^2 vs Nvdiffrec

Figure 8 and Figure 9 present a visual comparison of the convergence and accuracy of 3D reconstruction using different numbers of views with the Nvdiffrec and HI^2 methods. Figure 8 shows the progression of reconstruction over 100 iterations, comparing the output, reference, and normal. While the quality of Nvdiffrec improves with more views, HI^2 achieves a high level of detail and accuracy, even with few views. This demonstrates that HI^2 can achieve reliable reconstructions, outperforming Nvdiffrec in terms of convergence and model accuracy, particularly when fewer views are available. Figure 9 further illustrates this comparison by showing the reconstructed models alongside the ground truth. The green and red circles highlight areas showing that HI^2 produces higher detail and can achieve this with limited views. Together, these figures emphasize the robustness of HI^2 in generating accurate 3D reconstructions with limited input views.

4.5.2 HI^2 vs All

Figure 10 provides a visual representation of the reconstruction quality achieved by Nvdiffrec, IDR, and HI^2, along with their corresponding Chamfer distance values. The comparison clearly highlights the superior performance of HI^2, as it consistently achieves lower Chamfer distance values across varying numbers of input views. While both Nvdiffrec and IDR show improvement as the number of views increases, HI^2 maintains high reconstruction quality even with minimal input views. This demonstrates the robustness and scalability of HI^2 in handling diverse 3D reconstruction scenarios, particularly when input views are limited. Furthermore, HI^2 exhibits better structural preservation and detail fidelity, outperforming the competing methods across all tested configurations.

Figure 11 further supports this observation by showcasing the reconstructed models for each method, colour-coded based on Chamfer distance. The visual comparison clearly shows that HI^2 produces the highest quality reconstructions, with significantly lower Chamfer distance values and fewer artifacts compared to Nvdiffrec and IDR. Notably, when the number of input views is minimal, HI^2 maintains superior accuracy and detail preservation, outperforming the other methods. These results demonstrate that HI^2 delivers cleaner and more precise reconstructions, making it highly effective for real-world scenarios with sparse data.

5 CONCLUSION

In this work, we propose a novel pipeline that enables highly accurate 3D object reconstruction from a sparse set of images. We introduce a novel shell-sampling strategy that transforms the coarse reconstruction into an implicit representation, allowing

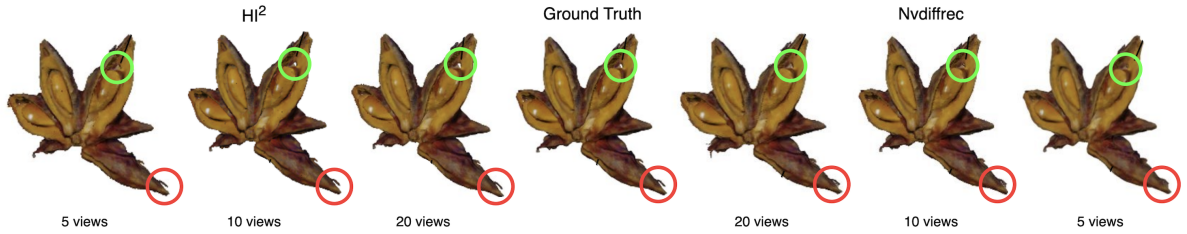

Figure 9: Visual comparison of 3D reconstructions using HI^2 and Nvdiffrec with varying numbers of views. The reconstructed models are shown alongside the ground truth, with green and red circles indicating areas of high accuracy and noticeable discrepancies, respectively. HI^2 consistently preserves fine details and maintains high accuracy, even with few views.

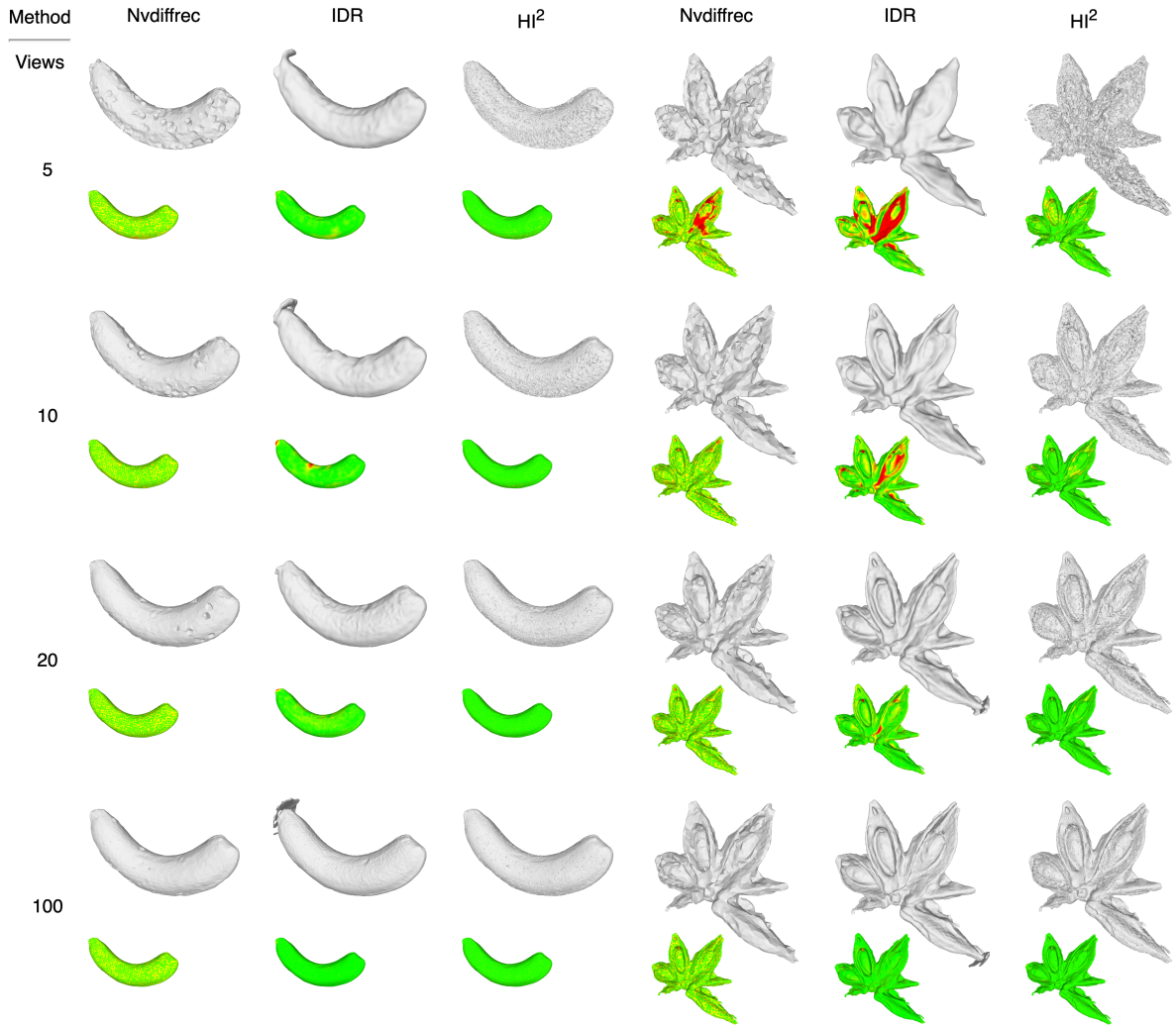

Figure 10: Qualitative comparison of 3D mesh reconstructions and Chamfer distance across different numbers of views (5, 10, 20, and 100) for OmniObject3D dataset. Results demonstrate that HI^2 achieves more accurate reconstructions compared to Nvdiffrec and IDR especially when limited views are available (5 or 10 images).

for further optimization by neural implicit rendering. Through our experiments, we demonstrate the effectiveness of our sampling strategy, which consistently outperforms state-of-the-art 3D reconstruction approaches across different multi-view setups. We believe our approach is not limited to only the Nvdiffrec pipeline but can also be integrated into other methods. Looking ahead, we aim to further improve

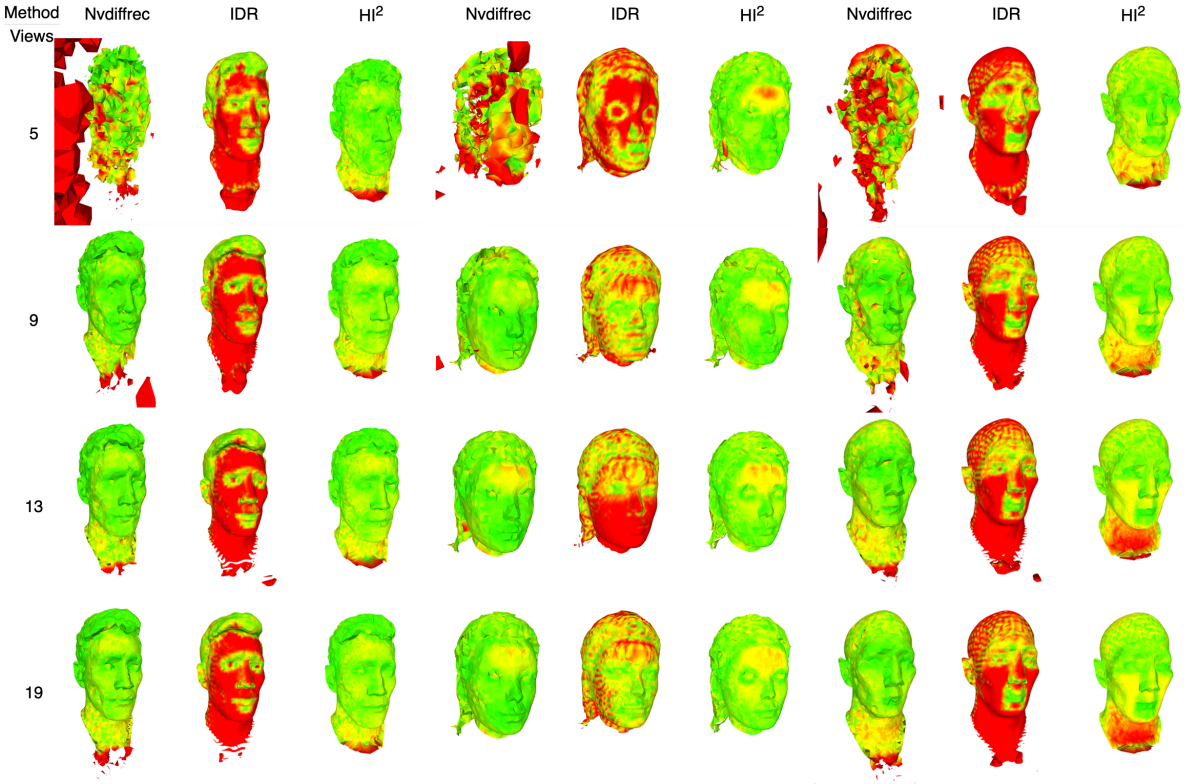

Figure 11: Qualitative comparison of Chamfer distance across different numbers of views (5, 9, 13, and 19) for face dataset. We can clearly see that for 5 images, Nvdiffrec did not converge, while HI^2 produced highly accurate results, outperforming both Nvdiffrec and IDR.

our pipeline to enable accurate 3D reconstruction with even fewer input images and integrate our initialization approach with other pipelines.

ACKNOWLEDGEMENT

This work was co-funded by the European Union under Horizon Europe, grant number 101092889, project SHARESPACE. We sincerely thank Dr. Bernd Krolla, Dr. Johannes Köhler, and Yongzhi Su for their mentorship and invaluable support throughout this research. We also extend our gratitude to Dr. Jason Rambach for his assistance in providing constructive feedback during the writing process.

REFERENCES

Besl, P. and McKay, N. D. (1992). A method for registration of 3-d shapes. *IEEE Transactions on Pattern Analysis and Machine Intelligence*, 14(2):239–256.

Bridson, R. and Doran, C. (2014). Quartet: A tetrahedral mesh generator that does isosurface stuffing with an acute tetrahedral tile. *https://github.com/crawforddoran/quartet*.

Choy, C. B., Xu, D., Gwak, J., Chen, K., and Savarese, S. (2016). 3d-r2n2: A unified approach for single and multi-view 3d object reconstruction. In *Computer Vision–ECCV 2016: 14th European Conference, Amsterdam, The Netherlands, October 11-14, 2016, Proceedings, Part VIII 14*, pages 628–644. Springer.

Community, B. O. (2018). *Blender - a 3D modelling and rendering package*. Blender Foundation, Stichting Blender Foundation, Amsterdam.

Dawson-Haggerty et al. trimesh.

Donne, S. and Geiger, A. (2019). Learning non-volumetric depth fusion using successive reprojections. In *Proceedings of the IEEE/CVF Conference on Computer Vision and Pattern Recognition*, pages 7634–7643.

Fridovich-Keil, S., Yu, A., Tancik, M., Chen, Q., Recht, B., and Kanazawa, A. (2022). Plenoxels: Radiance fields without neural networks. In *Proceedings of the IEEE/CVF Conference on Computer Vision and Pattern Recognition*, pages 5501–5510.

Furukawa, Y. and Ponce, J. (2009). Accurate, dense, and robust multiview stereopsis. *IEEE transactions on pattern analysis and machine intelligence*, 32(8):1362–1376.

Galliani, S., Lasinger, K., and Schindler, K. (2016). Gipuma: Massively parallel multi-view stereo recon-

struction. *Publikationen der Deutschen Gesellschaft für Photogrammetrie, Fernerkundung und Geoinformation e. V*, 25(361-369):2.

Garbin, S. J., Kowalski, M., Johnson, M., Shotton, J., and Valentin, J. (2021). Fastnerf: High-fidelity neural rendering at 200fps. In *Proceedings of the IEEE/CVF International Conference on Computer Vision*, pages 14346–14355.

Goesele, M., Curless, B., and Seitz, S. M. (2006). Multi-view stereo revisited. In *2006 IEEE Computer Society Conference on Computer Vision and Pattern Recognition (CVPR'06)*, volume 2, pages 2402–2409. IEEE.

Hartmann, W., Galliani, S., Havlena, M., Van Gool, L., and Schindler, K. (2017). Learned multi-patch similarity. In *Proceedings of the IEEE international conference on computer vision*, pages 1586–1594.

Inc., R. (2022). *Character Creator 4*. Version 4.0.

Jensen, R., Dahl, A., Vogiatzis, G., Tola, E., and Aanæs, H. (2014). Large scale multi-view stereopsis evaluation. In *2014 IEEE Conference on Computer Vision and Pattern Recognition*, pages 406–413. IEEE.

Jiang, Y., Ji, D., Han, Z., and Zwicker, M. (2020). Sdfdiff: Differentiable rendering of signed distance fields for 3d shape optimization. In *Proceedings of the IEEE/CVF Conference on Computer Vision and Pattern Recognition*, pages 1251–1261.

Kanazawa, A., Tulsiani, S., Efros, A. A., and Malik, J. (2018). Learning category-specific mesh reconstruction from image collections. In *Proceedings of the European Conference on Computer Vision (ECCV)*, pages 371–386.

Kar, A., Häne, C., and Malik, J. (2017). Learning a multi-view stereo machine. *Advances in neural information processing systems*, 30.

Kazhdan, M., Bolitho, M., and Hoppe, H. (2006). Poisson surface reconstruction. In *Proceedings of the fourth Eurographics symposium on Geometry processing*, volume 7, page 0.

Kellnhofer, P., Jebe, L. C., Jones, A., Spicer, R., Pulli, K., and Wetzstein, G. (2021). Neural lumigraph rendering. In *Proceedings of the IEEE/CVF Conference on Computer Vision and Pattern Recognition*, pages 4287–4297.

Kolmogorov, V. and Zabih, R. (2002). Multi-camera scene reconstruction via graph cuts. In *Computer Vision—ECCV 2002: 7th European Conference on Computer Vision Copenhagen, Denmark, May 28–31, 2002 Proceedings, Part III 7*, pages 82–96. Springer.

Kutulakos, K. N. and Seitz, S. M. (2000). A theory of shape by space carving. *International journal of computer vision*, 38:199–218.

Liu, S., Li, T., Chen, W., and Li, H. (2019a). Soft rasterizer: A differentiable renderer for image-based 3d reasoning. In *Proceedings of the IEEE/CVF International Conference on Computer Vision*, pages 7708–7717.

Liu, S., Saito, S., Chen, W., and Li, H. (2019b). Learning to infer implicit surfaces without 3d supervision. *Advances in Neural Information Processing Systems*, 32.

Liu, S., Zhang, Y., Peng, S., Shi, B., Pollefeys, M., and Cui, Z. (2020). Dist: Rendering deep implicit signed distance function with differentiable sphere tracing. In *Proceedings of the IEEE/CVF Conference on Computer Vision and Pattern Recognition*, pages 2019–2028.

Lorensen, W. E. and Cline, H. E. (1987). Marching cubes: A high resolution 3d surface construction algorithm. *ACM siggraph computer graphics*, 21(4):163–169.

Luo, K., Guan, T., Ju, L., Huang, H., and Luo, Y. (2019). P-mvsnet: Learning patch-wise matching confidence aggregation for multi-view stereo. In *Proceedings of the IEEE/CVF International Conference on Computer Vision*, pages 10452–10461.

Martin-Brualla, R., Radwan, N., Sajjadi, M. S., Barron, J. T., Dosovitskiy, A., and Duckworth, D. (2021). Nerf in the wild: Neural radiance fields for unconstrained photo collections. In *Proceedings of the IEEE/CVF Conference on Computer Vision and Pattern Recognition*, pages 7210–7219.

Mescheder, L., Oechsle, M., Niemeyer, M., Nowozin, S., and Geiger, A. (2019). Occupancy networks: Learning 3d reconstruction in function space. In *Proceedings IEEE Conf. on Computer Vision and Pattern Recognition (CVPR)*.

Mildenhall, B., Srinivasan, P. P., Tancik, M., Barron, J. T., Ramamoorthi, R., and Ng, R. (2021). Nerf: Representing scenes as neural radiance fields for view synthesis. *Communications of the ACM*, 65(1):99–106.

Munkberg, J., Hasselgren, J., Shen, T., Gao, J., Chen, W., Evans, A., Müller, T., and Fidler, S. (2022). Extracting triangular 3d models, materials, and lighting from images. In *Proceedings of the IEEE/CVF Conference on Computer Vision and Pattern Recognition*, pages 8280–8290.

Park, J. J., Florence, P., Straub, J., Newcombe, R., and Lovegrove, S. (2019). Deepsdf: Learning continuous signed distance functions for shape representation. In *Proceedings of the IEEE/CVF conference on computer vision and pattern recognition*, pages 165–174.

Pons, J.-P., Keriven, R., and Faugeras, O. (2005). Modelling dynamic scenes by registering multi-view image sequences. In *2005 IEEE Computer Society Conference on Computer Vision and Pattern Recognition (CVPR'05)*, volume 2, pages 822–827. IEEE.

Pumarola, A., Corona, E., Pons-Moll, G., and Moreno-Noguer, F. (2021). D-nerf: Neural radiance fields for dynamic scenes. In *Proceedings of the IEEE/CVF Conference on Computer Vision and Pattern Recognition*, pages 10318–10327.

Reiser, C., Peng, S., Liao, Y., and Geiger, A. (2021). Kilonerf: Speeding up neural radiance fields with thousands of tiny mlps. In *Proceedings of the IEEE/CVF International Conference on Computer Vision*, pages 14335–14345.

Riegler, G., Ulusoy, A. O., Bischof, H., and Geiger, A. (2017). Octnetfusion: Learning depth fusion from data. In *2017 International Conference on 3D Vision (3DV)*, pages 57–66. IEEE.

Schönberger, J. L., Zheng, E., Frahm, J.-M., and Pollefeys, M. (2016). Pixelwise view selection for unstructured multi-view stereo. In *Computer Vision–ECCV 2016: 14th European Conference, Amsterdam, The Netherlands, October 11-14, 2016, Proceedings, Part III 14*, pages 501–518. Springer.

Shen, T., Gao, J., Yin, K., Liu, M.-Y., and Fidler, S. (2021). Deep marching tetrahedra: a hybrid representation for high-resolution 3d shape synthesis. *Advances in Neural Information Processing Systems*, 34:6087–6101.

Shewchuk, J. R. (1998). An introduction to the conjugate gradient method without the agonizing pain. In *Proceedings of the 7th International Conference on Meshing Roundtable*, Meshing Roundtable, pages 3–17, Albuquerque, NM, USA. Sandia National Laboratories.

Tretschk, E., Tewari, A., Golyanik, V., Zollhöfer, M., Stoll, C., and Theobalt, C. (2020). Patchnets: Patch-based generalizable deep implicit 3d shape representations. In *Computer Vision–ECCV 2020: 16th European Conference, Glasgow, UK, August 23–28, 2020, Proceedings, Part XVI 16*, pages 293–309. Springer.

Wang, N., Zhang, Y., Li, Z., Fu, Y., Liu, W., and Jiang, Y.-G. (2018). Pixel2mesh: Generating 3d mesh models from single rgb images. In *Proceedings of the European conference on computer vision (ECCV)*, pages 52–67.

Wang, Z., Wu, S., Xie, W., Chen, M., and Prisacariu, V. A. (2021). Nerf–: Neural radiance fields without known camera parameters. *arXiv preprint arXiv:2102.07064*.

Wizadwongsa, S., Phongthawee, P., Yenphraphai, J., and Suwajanakorn, S. (2021). Nex: Real-time view synthesis with neural basis expansion. In *Proceedings of the IEEE/CVF Conference on Computer Vision and Pattern Recognition*, pages 8534–8543.

Wu, T., Zhang, J., Fu, X., Wang, Y., Ren, J., Pan, L., Wu, W., Yang, L., Wang, J., Qian, C., et al. (2023). Omniobject3d: Large-vocabulary 3d object dataset for realistic perception, reconstruction and generation. In *Proceedings of the IEEE/CVF Conference on Computer Vision and Pattern Recognition*, pages 803–814.

Yan, X., Yang, J., Yumer, E., Guo, Y., and Lee, H. (2016). Perspective transformer nets: Learning single-view 3d object reconstruction without 3d supervision. *Advances in neural information processing systems*, 29.

Yariv, L., Kasten, Y., Moran, D., Galun, M., Atzmon, M., Ronen, B., and Lipman, Y. (2020). Multiview neural surface reconstruction by disentangling geometry and appearance. *Advances in Neural Information Processing Systems*, 33:2492–2502.

Yu, A., Li, R., Tancik, M., Li, H., Ng, R., and Kanazawa, A. (2021). Plenoctrees for real-time rendering of neural radiance fields. In *Proceedings of the IEEE/CVF International Conference on Computer Vision*, pages 5752–5761.

Zhang, K., Riegler, G., Snavely, N., and Koltun, V. (2020). Nerf++: Analyzing and improving neural radiance fields. *arXiv preprint arXiv:2010.07492*.

APPENDIX

The DTU (Jensen et al., 2014) dataset is a well-known benchmark for 3D reconstruction, notable for its diversity in object types and challenging imaging conditions. Many images in the dataset capture objects partially only, resulting in incomplete views that can complicate reconstruction tasks.

Table 2 provides a quantitative comparison of PSNR values for two scans (scan40 and scan65) across different numbers of input views. HI^2 consistently outperforms both IDR and Nvdiffrec, achieving the highest PSNR values in every configuration. Its performance remains strong, especially with sparse input (e.g., 5 views), and delivers the best results for all tested view counts. Figure 12 visually compares

	scan40				scan65			
Views	5	10	20	49	5	10	20	49
IDR	21.87	21.84	23.03	25.11	21.33	22.08	20.27	23.21
Nvdiffrec	22.27	23.25	23.73	23.88	20.3	20.55	21.5	21.57
HI^2	**24.05**	**24.65**	**25.09**	**25.631**	**23.32**	**24.8**	**25.05**	**26.68**

Table 2: PSNR value ↑ for DTU dataset across the different number of views. The bolded values highlight the best performance for each view count and dataset combination.

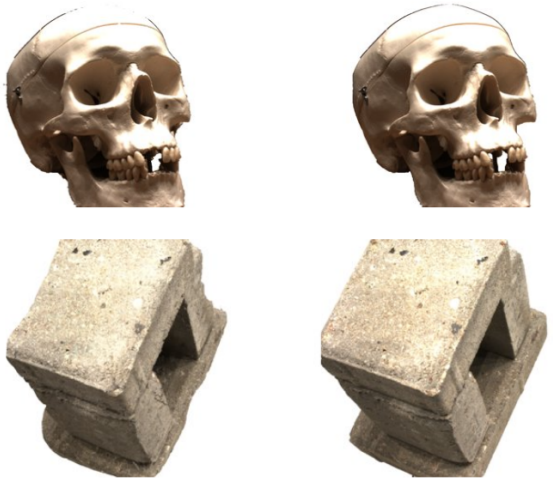

Figure 12: Results for the DTU dataset with 10 random images trained for 2000 iterations. We can see clearly we are able to produce results close to the ground truth.

reconstructions produced by HI^2 against the ground truth. Using only 10 input images and training for 2000 iterations, HI^2 achieves results that closely resemble the ground truth despite the challenges posed by the dataset. These results underscore HI^2 's ability to generate high-quality reconstructions even under constrained conditions, reaffirming its efficiency.